Smart Structures and Systems, *Vol. 24, No. 3 (2019) 303-317*
DOI: https://doi.org/10.12989/sss.2019.24.3.303

Characterizing nonlinear oscillation behavior of an MRF variable rotational stiffness device

Yang Yu*, Yancheng Li, Jianchun Li** and Xiaoyu Gu

Centre for Built Infrastructure Research, School of Civil and Environmental Engineering, University of Technology Sydney, 15 Broadway, Ultimo NSW 2007, Australia

(Received September 21, 2018, Revised August 4, 2019, Accepted August 10, 2019)

Abstract. Magneto-rheological fluid (MRF) rotatory dampers are normally used for controlling the constant rotation of machines and engines. In this research, such a device is proposed to act as variable stiffness device to alleviate the rotational oscillation existing in the many engineering applications, such as motor. Under such thought, the main purpose of this work is to characterize the nonlinear torque-angular displacement/angular velocity responses of an MRF based variable stiffness device in oscillatory motion. A rotational hysteresis model, consisting of a rotatory spring, a rotatory viscous damping element and an error function-based hysteresis element, is proposed, which is capable of describing the unique dynamical characteristics of this smart device. To estimate the optimal model parameters, a modified whale optimization algorithm (MWOA) is employed on the captured experimental data of torque, angular displacement and angular velocity under various excitation conditions. In MWOA, a nonlinear algorithm parameter updating mechanism is adopted to replace the traditional linear one, enhancing the global search ability initially and the local search ability at the later stage of the algorithm evolution. Additionally, the immune operation is introduced in the whale individual selection, improving the identification accuracy of solution. Finally, the dynamic testing results are used to validate the performance of the proposed model and the effectiveness of the proposed optimization algorithm.

Keywords: magneto-rheological fluid; variable stiffness device (VSD); rotational hysteresis model; parameter identification; whale optimization algorithm

1. Introduction

There are two types of magneto-rheological (MR) dampers categorized by their motion types, i.e. linear MR damper and rotary MR damper. The former has been extensively investigated from comprehensive angles, i.e., structural design (Christie *et al.* 2019, Hong *et al.* 2005, Sohn *et al.* 2015, Sun *et al.* 2015), experimental characterization (Dyke *et al.* 1998), parametric/non-parametric modeling (Nguyen and Choi 2010, Yu *et al.* 2013, Yang *et al.* 2002, 2004, Wang and Liao 2011, Spencer Jr *et al.* 1997, Truong and Ahn 2010, Chen *et al.* 2015), semi-active control strategies (Zhou *et al.* 2006, Braz-César and Barros 2018, Muthalif *et al.* 2017, Zhou *et al.* 2012, Li *et al.* 2002, Dyke *et al.* 1996), etc. Compared with its brother, the rotary MR damper has not been in the main spotlight (Imaduddin *et al.* 2013), despite it conquers some of the disadvantages of linear MR damper, i.e., large installation requirement, potential buckle of the rod at high speed, vulnerable to external contamination due to exposed rod and higher volume demand for MR fluid.

Huang *et al*. (2002) and Li and Du (2003) are among the early pioneers exploring the design and development of MR rotary dampers. Since then, extensive discussions and investigations on the device design have been conducted in the field, including single-disk type (Li and Du 2003), multiple-disk type (Park *et al.* 2006), use of multiple coils (Nguyen and Choi 2011), tailored disk surface (Nam and Ahn 2009), and magnetic circuit design (Nam *et al*. 2007). In review of the performance of MR rotary damper, most of the experimental testing is to examine the output torque of the damper against various constant rotation speeds with different applied currents. Experimental investigations have revealed that the generated torque of MR rotary damper is less sensitive to rotary speed which indicates that the MR rotary damper can be treated as variable stiffness device, though with small damping variation. As a consequence, the modeling efforts are focused on describing the performance of the MR rotary damper, i.e. output torque, with regard to a set of physical parameters (i.e. MR fluid property, disk radius, rod radius and gap size) and external stimulations (i.e., applied current and rotary speed) (Imaduddin *et al.* 2013). Those models, based on either Bingham plastic model (Song *et al.* 2013, Ehrgott and Masri 1992) or Herschel-Bulkley model (Wang and Gordaninejad 1999), are particularly useful for device design and controller design since they describe the steady behavior of MR rotary damper, i.e., constant rotary speed and applied current.

As a rotational variable stiffness device, MR rotary damper can also be used to mitigate the oscillatory

*Corresponding author, Ph. D.
E-mail: yang.yu@uts.edu.au
** Ph. D.
E-mail: jianchun.li@uts.edu.au

http://www.techno-press.com/journals/sss&subpage=7
ISSN: 1738-1584 (Print), 1738-1991 (Online)

vibrations (Gong *et al.* 2012, Li *et al.* 2003), shown in Fig. 1, as vibration isolator. Real-time varying rotational stiffness offers potential to isolate the transmission of the external vibration disturbance and therefore to protect the machinery and other equipment that is vulnerable to external vibrations. However, the exploration on this aspect especially the dynamic characteristics of MR rotary damper has been rarely reported. Tse and Chang (2004) proposed to use MR rotary damper for small-scale wind control application. They conducted oscillating experimental testing on a shear-mode MR rotary damper to capture its hysteric behavior. The original Bouc-Wen model was proposed to portray its nonlinear behavior. Li and Li (2014) proposed its use in structural control application, i.e. connecting the column and beam to adjust the structural stiffness, and experimentally tested the performance of a disk-type MR rotary damper under oscillating vibrations. A rotational hyperbolic model and a hybrid hysteresis model (Royel *et al.* 2015) were proposed to describe the behavior of the MR rotary damper. Furthermore, by 'locking' and 'unlocking' the connection, they demonstrated that the natural frequency of the structure equipped with MR rotary damper as joint element is capable of being shifted from 0.7 Hz to 1.2 Hz (72% change).

Although existing models are capable of describing dynamic behavior of MR-based rotary device in oscillatory motion, they still suffer from several problems in the engineering applications. First, the proposed Bouc-Wen-based model in (Tse and Chang 2004) has a total of 11 parameters to be identified, which requires a heavy computation resource to achieve high-accuracy identification results. Also, too many parameters will definitely affect the robustness of the designed controller, finally influencing the control effect in structural vibration mitigation. To lower the complexity of the model for MR rotary damper, a hybrid model was proposed in (Royel *et al.* 2015), consisting of a Gaussian function and a tangent hyperbolic function. Compared with the original Bouc-Wen model, this model just has as smallest as five parameters to be identified, avoiding a large number of parameters and nonlinear differential equation in the model expression. However, this model is not able to accurately capture the yielding points at the higher velocities when the loading frequency is over 2 Hz. Since the main seismic frequencies are generally in the range of 1-5 Hz, the hybrid hysteresis model is not suitable for the application of the device in the structural vibration control due to the earthquakes. One the other hand, the model parameter identification is also challenging if the proposed model structure is complex. Generally, the procedure of model parameter identification for MR rotary devices is considered as solving a global optimization problem, which can be implemented using evolutionary algorithms in the way that errors between experimental data and model predictions are minimized. Therefore, the model accuracy is closely associated with the model complexity and selected parameter identification algorithm. If the configuration of the model to be identified is too complicated, the optimization algorithm may fail to converge to optimal values of model parameters.

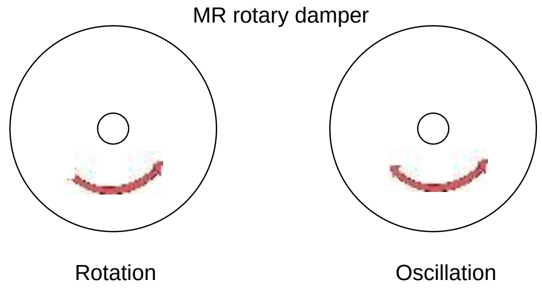

Fig. 1 MR rotary damper under rotation and oscillation

Furthermore, the priori information on the scales of parameters is desirable to enhance the algorithm convergence. In view of these issues, it is absolutely requisite to develop a simpler and more accurate model that is able to describe the nonlinear dynamics of MR rotary damper via the regulation of different model parameters.

In this study, dynamic tests on an MR fluid (MRF)-based variable stiffness device (VSD) are conducted under various loading conditions. Based on experimental results, a rotational hysteresis model, consisting of a rotational spring, a viscous dashpot and a hysteresis component, is proposed to characterize the dynamic response of MRF VSD. Compared with conventional models of MRF devices such as Bouc-Wen model (Spencer Jr *et al.* 1997) and LuGre friction model (Jiménez and Álvarez-Icaza 2005), the proposed model does not contain any differential equation and just has five parameters to be identified. Then, a newly developed swarm-based algorithm, whale optimization algorithm (WOA), is introduced to be considered as an ideal candidate for model parameter identification. To improve the convergence rate of parameter identification and avoid the local optimum of solution, a nonlinear updating strategy is adopted to balance the global and local search abilities of the algorithm. Moreover, the immune operation is added into the algorithm to realize optimal whale individual selection, improving the identification accuracy of WOA. The relationships between model parameters and supplying current are also investigated to set up a generalized field-dependent model, which is finally proved to be feasible in the control application using MRF VSD.

The reminder of this paper is given as following. The design description and dynamic tests of MRF VSD will be introduced in Section 2 together with the analysis of captured nonlinear responses. Section 3 presents the rotational hysteresis model as well as problem statement for model parameter identification. A modified WOA and its procedure for parameter identification are described in detail in Section 4. Section 5 assesses the performance of the proposed model, and discusses the effectiveness of the modified WOA through the comparison with other homologous optimization algorithms. Eventually, a conclusion is addressed in Section 6.

2. Variable rotational stiffness device

2.1 Design of MRF VSD

A disk-type MRF VSD was developed and prototyped as an intelligent structural component, in which the torque resistance of the device is able to be instantaneously tuned according to the applied electricity current (Li and Li 2014). It is principally made up of two matching housings to construct the empty hole, the rounded coils to generate the magnetic fields for the magnetization of MRFs, a shaft that is connected with a rotational thin plate therein to transmit the torque of the device and smart materials (MRFs) between the plate and housing, which is shown in Fig. 2 (a) and (b). Two bearings are installed between the housing and shaft to guarantee the rotational movement of the device. The gap between the housing and the plate is around 1 mm to support the MRFs (MRF140GG, Lord Corp) inside the device, which are capable of providing the yield stress as high as 60,000 Pa at the saturated magnetic field of 1 T. Accordingly, the device is able to generate around 15 Nm of torque with the saturated current of 2 A because of good shear performance of MRFs.

Due to the distinct characteristics of MRF, the MRF VSD can change the torque resistance in real-time given the changeable magnetic fields. In addition, this device has the benefits of low energy consumption (Zhu *et al.* 2012), easy installation and quick response, which make the physical properties of the intelligent structure with the smart device, such as damping and stiffness, instantly field-controllable.

2.2 Dynamic test of MRF VSD

To evaluate and characterize the nonlinear torque-angular/angular velocity responses of MRF VSD, a series of tests are carried out in the Structures Laboratory at University of Technology Sydney. Because this device is generally used as a joint connector, it is of great necessity to evaluate its dynamic performance against horizontal loadings. When the structure is experiencing hazard external loading, i.e. strong wind, earthquake, etc., the major movement in the structural elements attached to the MRF VSD is the horizontal movement of the adjacent beam. Therefore, a uniaxial shake table, with the capacity of 10 T and scale of 3×3 m^2, is utilized to simulate the horizontal motion of the floor plate. Additionally, unlike conventional MR rotary dampers, the angular movement in MRF VSD as a joint is relatively small (less than 15 degrees), so the proposed experimental setup (shown in Fig. 3) is more favourable, in which the MRF VSD is installed on the ground by a supporter. Two steel plates and a steel rod are utilized to attach the device to the shake table. The load cell (Model No CSBA-500L, Curiosity Technology Co. Ltd), connected to the rod, is used to gauge the generated forces to the smart device. The current amplifier (Model No ADA4312, ANALOG DEVICES) is employed to generate the current to the electromagnetic coil of the device to produce satisfying magnetic field. Two LPS displacement transducers (Model No LIPS 117, POSITEK), with the scale of 5-350 mm, are also adopted to respectively gauge the vertical and horizontal displacements of the rod tip. The dSPACE is employed to control and monitor the generated electricity current.

During the tests, various sinusoid excitations are chosen to drive the MRF VSD. The loading amplitude ranges from 7.06 mm to 28.20 mm, corresponding to the maximal rotatory angles of 2, 5 and 8 degrees. The excitation frequencies are selected as 0.5 Hz, 1 Hz, 2 Hz and 3 Hz, because the dominant seismic frequencies are in the range of 0.1-5 Hz. To evaluate the current-dependent capacity of the device, five current levels are used to energize the MRF VSD, i.e. 0 A, 0.5 A, 1 A, 1.5 A and 2 A.

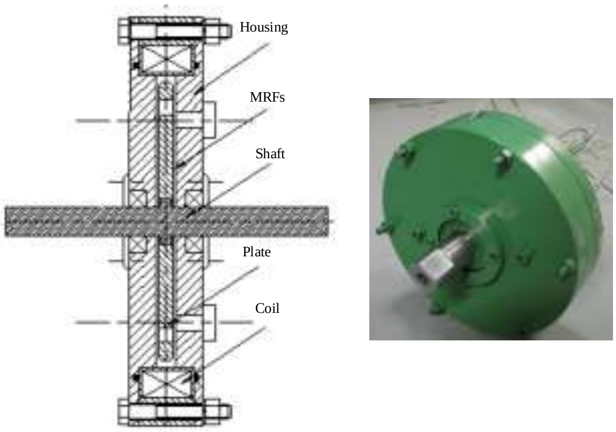

(a) Cross-section view (b) Real objective

Fig. 2 Design and prototype of MRF VSD

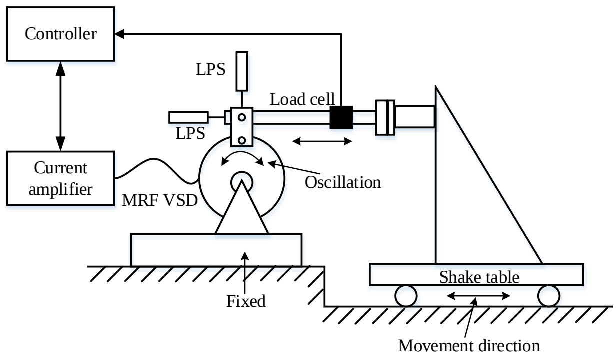

(a) Sketch of experimental setup

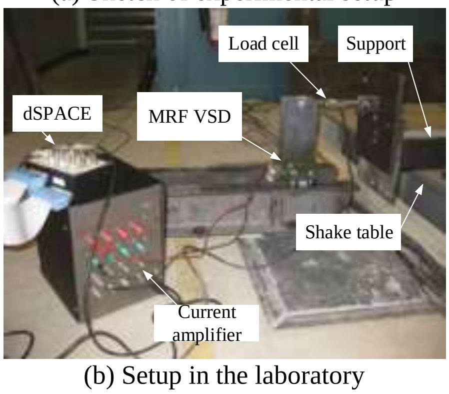

(b) Setup in the laboratory

Fig. 3 Experimental setup for dynamic testing of MRF VSD

During the test, the sampling frequency is set as 2048 Hz to fully get the dynamic characteristics of the device. The data collected during the testing are recorded by a local computer for model development and validation. To guarantee a stable performance of the MRF VSD, more than 5 cycles are gauged for every loading condition. Temperature of the device is controlled as the same level for each test.

2.3 Nonlinear response of MRF VSD

Fig. 4 shows an example of measured dynamic responses of MRF VSD with different current levels when it is excited by the harmonic loadings with 2 Hz frequency and 17.54 mm amplitude. The torque-angular displacement responses are described in Fig. 4(a) while Fig. 4(b) presents the relationships between torques and angular velocities. It is clearly seen that the hysteresis loops steadily increase with the adding current level, reflecting in the enclosed area of the responses. When there is no current applied to the device, the relationship between the torque and angular displacement shows almost elliptic, which signifies the device with viscous characteristic. With the increase of applied current level, it is evident that the slopes of both torque-angular displacement and torque-angular velocity loops linearly ascend.

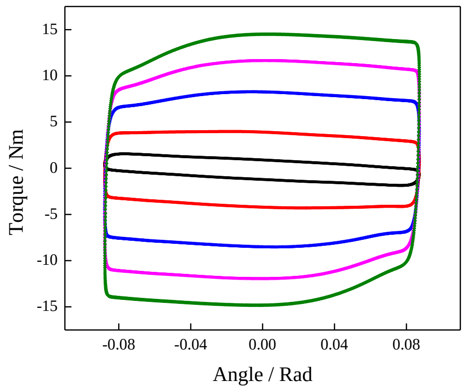

(a) Torque-angular displacement responses

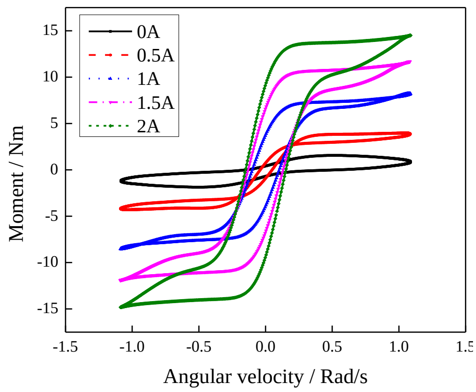

(b) Torque-angular velocity responses

Fig. 4 Nonlinear responses of MRF VSD supplied with different current levels (2Hz-17.65 mm)

3. Dynamic modeling of MRF VSD

3.1 The rotational hysteresis model

The main challenge of modeling this device is how to account for highly nonlinear and hysteretic behavior of MRF material. As described in Fig. 4, the MRF VSD exhibits the response features of MRF with close linearity at pre-yield regions, torque roll off phenomenon at low angular velocities and hysteretic effect at post-yield regions. Accordingly, the characterization of MRF VSD can refer to existing models of MRF or other MRF-based device. In (Wereley *et al.* 1999, Hu and Wereley 2008), to perfectly portray the unique behaviors of MRF damper at pre-yield and post-yield regions, a stiffness-viscosity-elasto-slide model was proposed, consisting of the linear combination of a linear stiffness component, a linear viscous dashpot component and a nonlinear elasto-slide component. In this model, the dashpot and spring components are used to provide linear damping and essential slope to the hysteretic responses of MRF damper while the elasto-slide component is employed to describe the stiffness in the area where the velocity varies the sign.

In the same way, the developed model for MRF VSD will follow the structure of the stiffness-viscosity-elasto-slide model due to similar features of response curve caused by MRF material. Fig. 5 gives the response decomposition of a typical torque-angular velocity loop of MRF VSD. It is noticeable that the response curve can be decomposed into three separate sub-curves associated with different components in the model: rotational stiffness component, rotational damping component and an *S*-shape component. Therefore, the developed model with such type of structure is feasible to describe the nonlinear and hysteretic responses of MRF VSD. However, there are a large number of functions that can be selected to illustrate the *S*-shape curve, such as hyperbolic tangent function, arctangent function, the Gauss error function, algebraic function and logistic function. Fig. 6 gives the curve shapes of different *S*-curve functions. In this work, the Gauss error function is selected due to the steepest slope among all the curves, which fits well with the change tendency of torque-angular velocity response of MRF VSD under harmonic excitations. As a result, the specific model configuration and expression can be demonstrated by Fig. 7 and Eqs. (1) and (2):

$$T(t) = k(f,A,I)\cdot\theta(t) + c(f,A,I)\cdot\dot{\theta}(t) + \alpha(f,A,I)\cdot y + T_0 \qquad (1)$$

$$y = \mathrm{erf}\big[\beta(f,A,I)\cdot\dot{\theta}(t) + \gamma(f,A,I)\cdot sign\big(\theta(t)\big)\big] \qquad (2)$$

where f, A and I denote excitation frequency, amplitude and applied current, respectively; θ and $\dot{\theta}$ denote the angular displacement and angular velocity, respectively; T denotes the device torque resistance; T_0 denotes the initial torque resistance of the device, which can be calculated via averaging the maximum and minimum values of captured torques under each excitation condition; k and c denote the rotational stiffness and damping coefficients, respectively; α denotes the hysteretic scale coefficient; β is a parameter to determine the slope of torque-angular velocity response; γ is

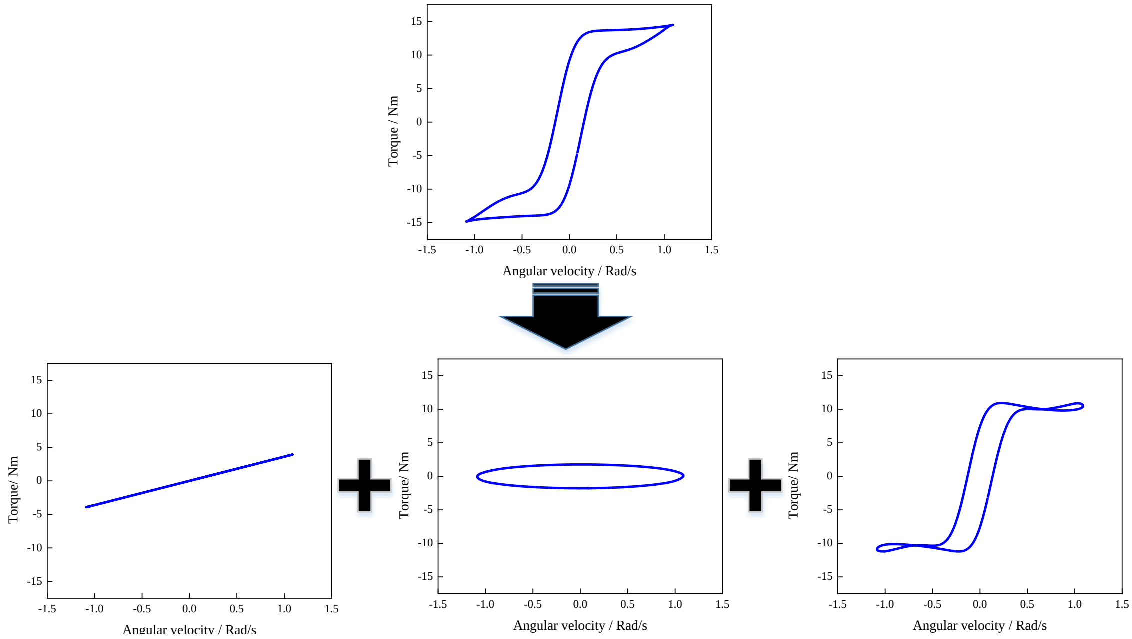

Fig. 5 Decomposition of the output response of MRF VSD

a parameter that is used together with sign of angular displacement to define the width of the *S*-shape hysteresis; erf(·) denotes the Gauss error function with the following expression

$$\operatorname{erf}(x)=\frac{1}{\sqrt{\pi}}\int_{-x}^{x}e^{-t^2}dt \tag{3}$$

In this model, the term $k{\cdot}\theta$ accounts for the opening observed from the area of zero angular velocity in the response; the term $c{\cdot}\dot{\theta}$ is used to describe the post yield relationship between angular velocity and joint torque resistance; α is designed to scale the whole hysteresis via adjusting the height of the hysteretic loop; β is a coefficient of the angular velocity of MRF VSD to regulate the slope of the hysteresis loop; γ is a parameter to control the width of the hysteresis loop via the angular displacement sign (sign($\theta(t)$)). Among them, k, c, α, β and γ are parameters to be identified, the values of which are associated with external loading conditions such as excitation frequency f, amplitude A and applied current level I to the device.

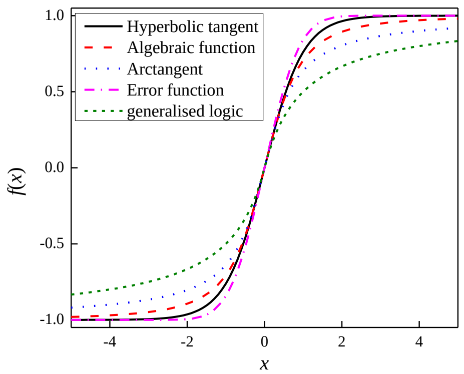

Fig. 6 *S*-shape performances of different functions

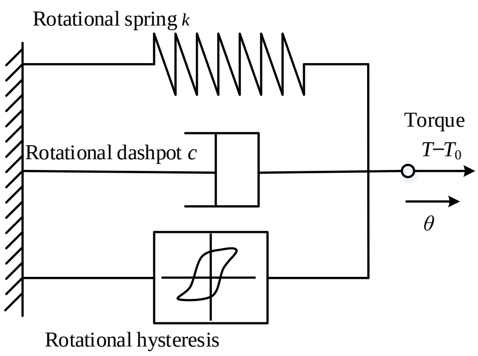

Fig. 7 The proposed rotational hysteresis model

3.2 Model identification

Parameter identification of the proposed model is deemed as solving a global optimization problem, in which the optimal values of model parameters can be obtained via minimizing the errors between experimental measurements and model predictions. In this work, the procedure of model identification will be divided into two phases. In the first phase, model parameters, considered as constant values, are identified under each loading condition. In the second phase, the relationships between parameters and excitation frequency and amplitude as well as applied current are investigated, contributing to a generalized rotational hysteresis model. Here, mean square error (MSE) between testing data and model outputs in one sampling cycle is selected as the objective function $H(X)$, shown as follows

$$H(X)=\frac{1}{N}\sum_{i=1}^{N}[T_{\exp}(i)-T(i)]^2 \tag{4}$$

$$T(i) = k \cdot \theta(i) + c \cdot \dot{\theta}(i) + \alpha \cdot y(i) + T_0 \tag{5}$$

$$y(i) = \mathrm{erf}[\beta \cdot \dot{\theta}(i) + \gamma \cdot sign(\theta(i))] \tag{6}$$

where $T_{exp}(i)$, $\theta(i)$ and $\dot{\theta}(i)$ denote the captured torque resistance, angular displacement and angular velocity at time t_i, respectively. If the value of the objective function is minimized to 0, the corresponding solution X=[k, c, α, β, γ] will be the optimal values of model parameters for MRF VSD. Due to the nonlinear relationships among identified parameters, the optimization algorithm is employed to calculate the optimal solution and the proposed method will be detailed in the next section. The schematic of model parameter identification for MRF VSD is shown in Fig. 8.

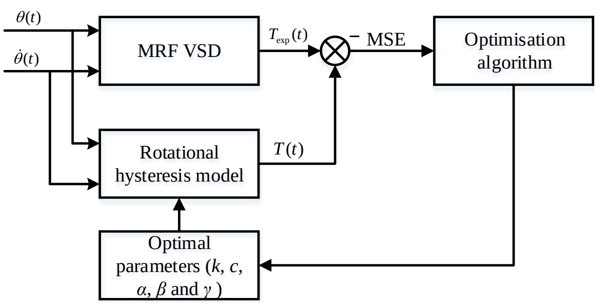

Fig. 8 Schematic of model parameter identification for MRF VSD

4. Methodology

4.1 Outline of whale optimization algorithm

Inspired by the foraging behavior of humpback whale swarm, Mirjalili and Lewis (2016) developed a meta-heuristic algorithm – whale optimization algorithm (WOA) as an effective tool to solve engineering optimization problems. Since humpback whales like hunting small fish herds and krill near the surface, they can produce unusual bubbles in a spiral shaped way close to the prey and in the meantime swim towards the preys. The WOA has three operations to imitate the humpback whales' behaviors of shrinking encircling prey, bubble-net attacking and search for prey. The detailed description and formulation of each operation is proved as follows.

1) Encircling prey. In the whale swarm, the present optimal individual is regarded as the objective of prey and other candidates will swim towards it via updating their locations according to the following equations.

$$\mathbf{X}(n+1) = \mathbf{X}_{opt}(n) - \mathbf{A} \cdot \mathbf{D} \tag{7}$$

$$\mathbf{D} = \left| \mathbf{C} \cdot \mathbf{X}_{opt}(n) - \mathbf{X}(n) \right| \tag{8}$$

$$\mathbf{A} = 2\mathbf{a} \cdot \mathbf{r} - \mathbf{a} \tag{9}$$

$$\mathbf{C} = 2 \cdot \mathbf{r} \tag{10}$$

where n denotes the current iteration number, $\mathbf{X}$ denotes the location vector, $\mathbf{X}_{opt}$ denotes the location vector of best individual at present, $\mathbf{A}$ and $\mathbf{C}$ denote coefficient vectors, $\mathbf{a}$ denotes the vector with linearly declining elements from 2 to 0 during the algorithm iteration, and $\mathbf{r}$ denotes the random number vector with the element values between 0 and 1.

2) Bubble-net attacking. Two methods are utilized to simulate this exploitation behavior of whales. First, a shrinking encircling mechanism is introduced based on random numbers in the sector $\mathbf{A}$ as illustrated in Eq. (9). The new location of a whale is able to be determined anywhere between original location of this whale and the location of current best one. Second, a spiral strategy is employed to update the locations of whales to simulate a helix shaped activity of whale swarm, shown in the following equation

$$\mathbf{X}(n+1) = \mathbf{D}' \cdot e^{bl} \cdot \cos(2\pi l) + \mathbf{X}_{opt}(n) \tag{11}$$

$$\mathbf{D}' = \left| \mathbf{X}_{opt}(n) - \mathbf{X}(n) \right| \tag{12}$$

where $\mathbf{D}'$ denotes the distance between whale and the prey (currently optimal solution), b denotes a constant parameter that is used to regulate the shape of the logarithmic spiral, and l denotes the random number between -1 and 1. To obtain an optimal performance, a probability of 0.5 is selected to optimize the locations of humpback whales between shrinking encircling operation and spiral strategy.

3) Search for prey. In this phase, the vector $\mathbf{A}$ with random values will be evaluated. If the $\mathbf{A}$ is more than 1 or less than -1, the locations of whales will be updated in accordance with a randomly selected individual rather than the optimal agent at present. The corresponding equations are given as follows

$$\mathbf{X}(n+1) = \mathbf{X}_{rand}(n) - \mathbf{A} \cdot \mathbf{D} \tag{13}$$

$$\mathbf{D} = \left| \mathbf{C} \cdot \mathbf{X}_{rand}(n) - \mathbf{X}(n) \right| \tag{14}$$

where $\mathbf{X}_{rand}$ is randomly selected from the whale swarm at the present iteration. The further details on WOA can be found in (Mirjalili and Lewis 2016).

4.2 Modified whale optimization algorithm

Although standard WOA is simple and easy to understand and implement, it always suffers from the problem of premature that may make the algorithm fall into the local optimum when dealing with the complicated global optimization problems (Su *et al.* 2018). The main reason contributing to this phenomenon is the diversity of the whale swarm. Because the initial locations of humpback whales are randomly selected, it may generate non-uniform distribution of the whale swarm, leading to poor global search ability of the algorithm. In this study, to solve this problem and improve the accuracy of the solution, a modified WOA (MWOA) is proposed, in which two significant improvements have been made and incorporated into the standard WOA.

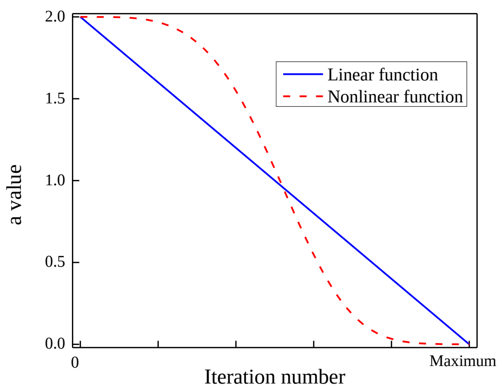

Fig. 9 Comparison between linear and nonlinear decreasing functions

The first modification is to replace the linearly decreasing coefficient a with a nonlinear updating mechanism, in which coefficient a is defined as a nonlinear function of iteration number. Fig. 9 gives an example of the comparison between linear and nonlinear decreasing functions. It is noticeable that compared with linear function, the nonlinear one can keep a slowly descending speed in the early stage of iteration and reach its minimal value much quickly in the later stage. In that case, elements in vector **A** generally have the big values initially and have small values at the end of algorithm iteration. As a consequence, in the initial iterations, the humpback whales have more chances to conduct the exploration behavior and search for prey (|**A**|≥1) so that it benefits the algorithm with a big search space to easily find the rough location of global optimum and avoid the search in the local region. However, in the later stage of evolution, the whales have more opportunities to conduct the exploitation behavior (|**A**|<1) so that the local research ability of WOA will be enhanced which can guarantee the algorithm accurately find the global optimum with faster convergence. Several nonlinearly decreasing functions have been proposed in previous studies for different engineering applications. In this work, a type of sigmoid function is chosen as the transfer function due to its outstanding nonlinear prediction ability, the expression of which is shown as

$$a = 2 \cdot e^{-10 \cdot (\frac{n}{N})^4} \tag{15}$$

where n and N denote the current and maximum iteration numbers, respectively.

The second modification is the introduction of immune operation to keep the best individuals in the whale swarm. Because bubble-net attacking behavior is a random process, the humpback whales tend to be premature convergence and fall into the local optimum. To prevent this problem, immune operation is employed in the MWOA, which is on basis of vertebrate immune system with an organism which protects itself from external disease. In this operation, the fitness function and corresponding solution are regarded as antigen and antibody, respectively. The match-degree between fitness and solution is represented by the proximity degree (affinity) between antigen and antibody, which causes the candidate antibodies to evolve. The similarity between every pair of solutions is represented by the concentration between corresponding antibodies, which can be used to monitor the diversity of the whale swarm. Accordingly, it is promising that the immune operation is added into the WOA to prevent the phenomenon of premature convergence.

For the ith humpback whale, its location x_i is represented by the antibody corresponding to the possible solution of the optimization problem. And the best location (prey) is represented by the antigen. Because the diversity of the whale swarm will be descended during the algorithm evolution, it is essential to preclude these antibodies with high concentrations for next-round iteration. In this study, the Euclidean distance is adopted to evaluate the proximity degree between a pair of antibodies: suppose fitness values of antibodies x_i and x_j are denoted by $f(x_i,c_i)$ and $f(x_j,c_j)$, and the proximity degree and concentration will be expressed by the following equations

$$p(x_i) = \sum_{j=1}^{M} \left| f(x_i, c_i) - f(x_j, c_j) \right| \tag{16}$$

$$Dy(x_i) = \frac{1}{p(x_i)} \tag{17}$$

where M denotes the antibody number and its value is 10 in this study; $p(x_i)$ and $Dy(x_i)$ denote the proximity degree and concentrate between antibody x_i and other antibodies. It is clearly seen that the larger the value of $p(x_i)$ is, the smaller the $Dy(x_i)$ will be. Based on $p(x_i)$ and $Dy(x_i)$, a selection probability of antibody x_i is defined as

$$sp(x_i) = \frac{p(x_i)}{\sum_{i=1}^{M} p(x_i)} = \frac{\sum_{j=1}^{M} \left| f(x_i, c_i) - f(x_j, c_j) \right|}{\sum_{i=1}^{M} \sum_{j=1}^{M} \left| f(x_i, c_i) - f(x_j, c_j) \right|} \tag{18}$$

According to the above equation, it is obvious that antibodies with high concentrations have low probabilities to be selected. Otherwise, it will be selected with high probabilities. In this way, poor antibodies are excluded via the selection strategy. Then, the antibodies with high fitness values are used to produce new antibodies as the elements of the cloning set, which is able to guarantee the diversity of the humpback whales via the replacement of excluded antibodies.

4.3 Model parameter identification based on MWOA

In this work, the MWOA is employed to estimate the optimal parameters of proposed rotational hysteresis model of MRF VSD. The detailed procedure of model identification, shown in Fig. 10, is described as follows:

Step 1. Determine the fitness function of the optimization problem and parameter setting of MOWA. In this research, the fitness function is given by Eq. (4) and algorithm parameters can be adjusted by trials according to the specific problem.

Step 2. Randomly initialize the locations of each humpback whale, set current iteration number n=1, and update **r**, **a**, **A**, **C**, l and p according to Eqs. (9)- (11) or random generation.

Step 3. Update the locations of whales. Judge the value of p: if p≥0.5, the humpback whales will execute bubble-net attacking behavior and update their locations according to the spiral Eq. (11). Or else, evaluate the absolute value of **A**. If |**A**|<1, update the whales' location using Eqs. (7) and (8); if |**A**|≥1, the search for prey behavior will be conducted and the locations of humpback whales will be updated by Eqs. (13) and (14).

Step 4. Check whether each individual gets out of the search space and modify it.

Step 5. Calculate the fitness of each whale and compare it with the current optimal fitness value. If the calculated fitness is better than current optimal one, record this fitness value and corresponding location X as best fitness and X_{opt}.

Step 6. After the pre-set N_d iterations, if the optimal fitness is not changed, carry out the immune operation. Here, N_d is set as 30.

Step 7. Calculate the selection probabilities of each candidate according to Eqs. (16)-(18). Then, based on the probabilities, the candidates with high fitness values will be employed to generate new individuals to replace the poor ones based on clonal proliferation operation.

Step 8. Evaluate the stopping criteria. In this study, the maximum iteration number N is seemed as the stopping condition. If the current iteration number is larger than the maximum value (n>N), the algorithm evolution will be stopped and the optimal solution will be outputted. Otherwise, n=n+1 and move to Step 2 to re-update **r**, **a**, **A**, **C**, l and p.

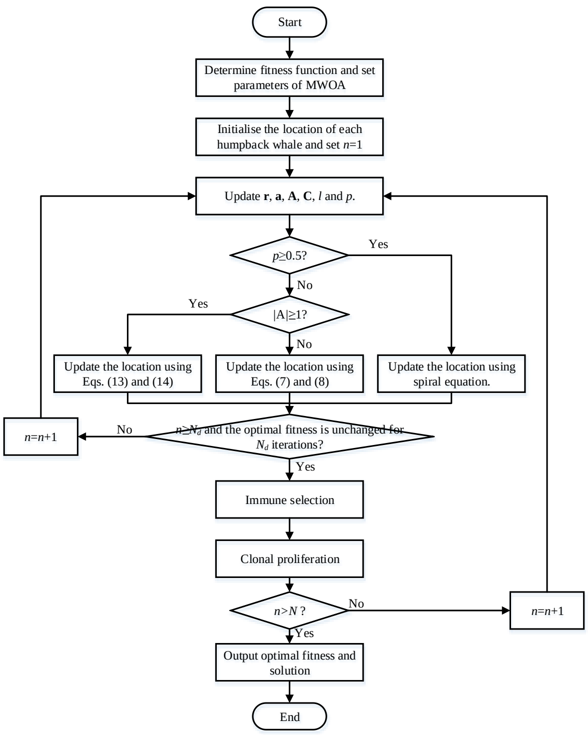

Fig. 10 Algorithm procedure of MWOA to identify the model parameters

5 Results and discussions

5.1 Algorithm setting and evaluation

The MWOA is implemented based on MATLAB v.2015a, in which there are three important algorithm parameters to be determined before the MWOA is adopted to identify the proposed model of MRF VSD, i.e., population number of humpback whale N_{pop}, maximum iteration number N and parameter to define the shape of logarithmic spiral b. Previous study suggested that b is not a very sensitive parameter associated with algorithm performance (Kaveh and Ghazaan 2017). Consequently, its value should be determined first given the fixed N_{pop} and N. In this part, the values of N_{pop} and N are selected as 30 and 400 according to (Kaveh and Ghazaan 2017). Fig. 11 gives the mean MSE of identification results using MWOA with different values of b. From the figure, it is noticeable that the value of MSE does not change too much with the different values of b from 0.5 to 2. However, comparison result shows that 1.2 should be most reliable value that contributes to a small MSE (0.0616). Then, the value of b is fixed to 1.2 and the influences of population number and maximum iteration on MSE are investigated. Here, various population numbers of humpback whale range from 10 to 50 with an interval of 10 while the maximum iteration numbers are chosen as 300, 400, 500, 600, 700, 800, 900 and 1000. Fig. 12 shows the graph of mean MSEs under different combinations of population number and maximum iteration number. It is apparent that the higher N_{pop} and N can result in better MSE result but require more calculation time meanwhile. Especially when the population number is over 30 or the maximum iteration number is over 600, the RMS changes less with the increasing values. As a consequence, to reduce the calculation amount, the optimal combination of population number and maximum iteration number is selected as (40, 800), corresponding to the MSE of 0.0613.

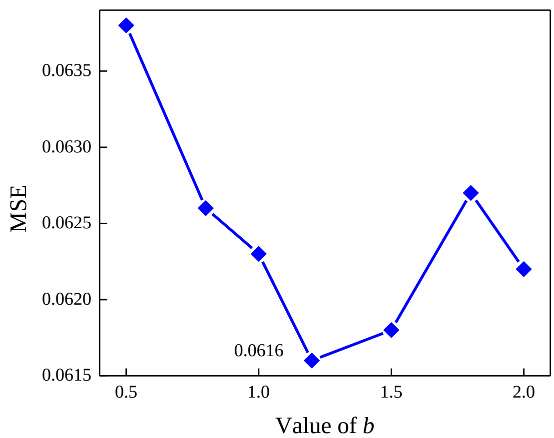

Fig. 11 Effect of parameter b on algorithm fitness

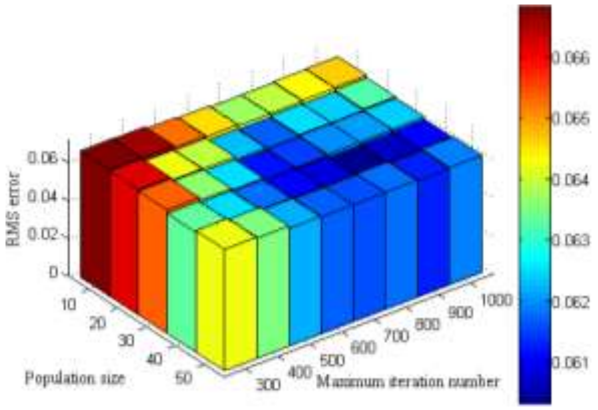

Fig. 12 Effects of population size and maximum iteration on algorithm fitness with fixed *b*

In order to prove the superiority of the MWOA over other commonly used optimization algorithms in parameter identification of the proposed model, a comparative study is conducted based on experimental data collected from the device with 3 Hz frequency and 17.65 mm amplitude excitation together with 1 A supplying current. In addition to MWOA, four common optimization algorithms, WOA, GA, PSO and monkey algorithm (MA), are selected for this investigation. MSE value and convergence rate are employed as evaluation indices to indicate the algorithm performance. To make a fair assessment, the population size and maximum iteration of all the algorithms are set as 40 and 800, respectively. Other parameter setting of each algorithm can be referred in (Li Voti 2018, Fesharaki and Golabi 2016, Yi *et al.* 2015). Fig. 13 illustrates the comparison result of convergence rates of different optimization algorithms. It is noted that PSO has the worst performance among all the testing algorithms in terms of MSE. The main reason contributing to this phenomenon is that in the PSO, the algorithm iteration is mainly dependent on initial solution scale. If the particles search the optimal solution in a relatively large space, the PSO is easy to fall into the local optimum, leading to the worse identification accuracy. Although MWOA reaches his optimal solution a little more slowly than WOA, GA and MA, it has the best fitness value, which is due to the local adjustment in the later stage of algorithm evolution. Accordingly, the MWOA can be regarded as a promising tool to identify the parameters of the proposed rotational hysteresis model for MRF VSD.

5.2 Model identification results

Based on the proposed MWOA with selected parameters in Section 5.1, the parameters of the rotational hysteresis model are identified for all the loading conditions, part results of which are shown in Figs. 14-16. Fig. 14 demonstrates the performance of the proposed model to predict the torque responses of the device with different applied current levels when the excitation condition is 1 Hz frequency and 7.06 mm amplitude. As can be seen from the figure, the increasing current can result in the adding nonlinear torque-angular velocity responses of the device. Five groups of comparisons between model predictions and experimental results have verified the effectiveness of this rotational hysteresis model to capture the responses with the adding current. Particularly, in each response loop, the reconstructed hysteresis fits well with the nonlinear phenomenon of the responses.

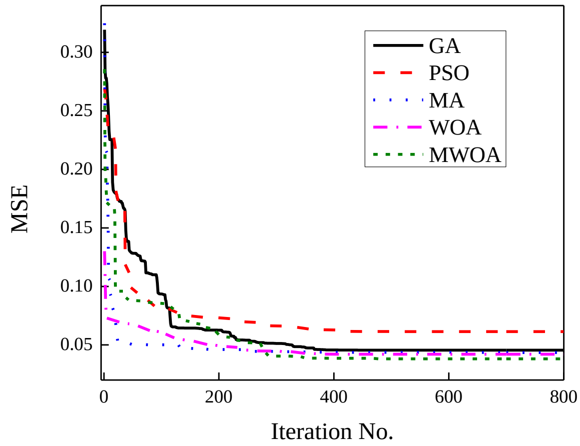

Fig. 13 Algorithm performance evaluation

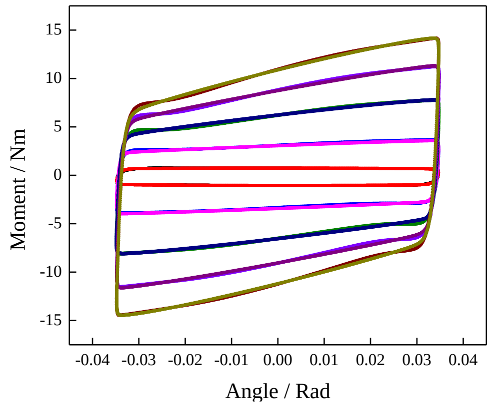

(a) Torque-angular displacement responses

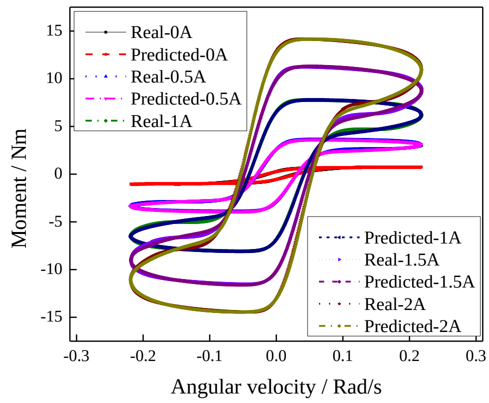

(b) Torque-angular velocity responses

Fig. 14 Response comparisons between experimental data and model predictions under different applied currents (7.06 mm – 1 Hz)

Fig. 15 investigates the ability of the model to describe the frequency-dependent feature of the device. In this study, the device is driven by 17.65 mm loading amplitude and supplied with 1 A current. The excitation frequency ranges from 0.5 Hz to 3 Hz. The results obviously show that the loading frequency has little effect on maximum torque of the responses. However, the ascending frequency will induce the growing nonlinear torque-angular velocity relationship. The perfectly matched loops in the figure illustrate that this model is capable of accurately portraying the frequency dependent phenomenon of the MRF VSD.

Fig. 16 compares the reconstructed responses with measured responses of the device with 0.5 Hz excitation frequency, 1.5 A applied current and different loading amplitudes, i.e., 7.06 mm, 17.65 mm and 28.2 mm. It is clearly seen that the hysteresis loops exhibit the shape of irregular rectangular with dull turns at right bottom and left top corners, which demonstrates the effect of the angular velocity on the device responses. Apparently, the angular velocity has little impact on peak value of torque but will affect the shape of response loops, as described in Fig. 16(b). Good agreements between experimental and reconstructed responses effectively validate the ability of the proposed model to describe this characteristic of the device.

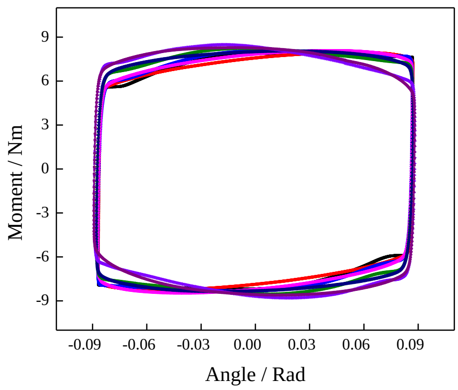

(a) Torque-angular displacement responses

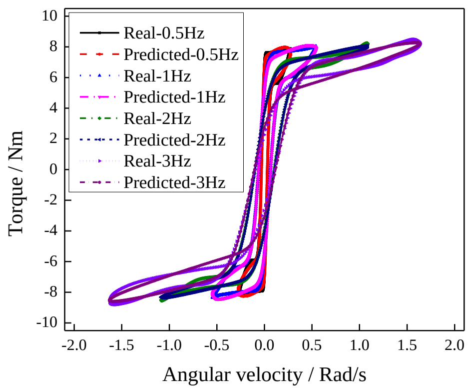

(b) Torque-angular velocity responses

Fig. 15 Response comparisons between experimental data and model predictions under different loading frequencies (17.65 mm – 1 A)

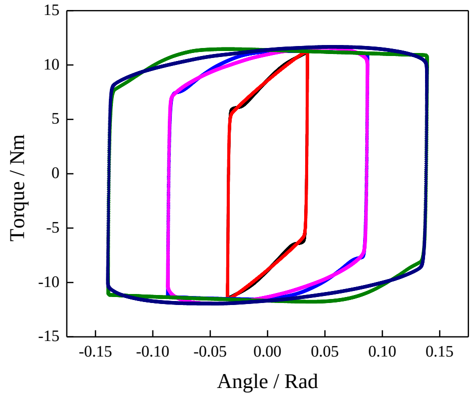

(a) Torque-angular displacement responses

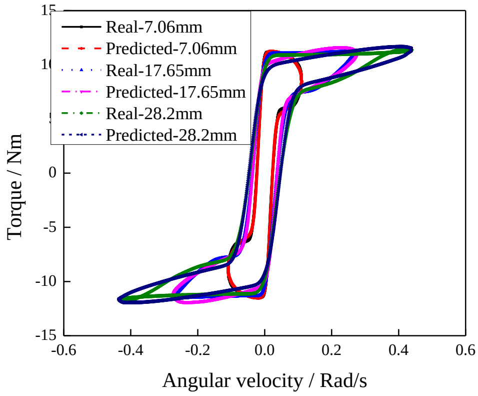

(b) Torque-angular velocity responses

Fig. 16 Response comparisons between experimental data and model predictions under different loading amplitudes (0.5 Hz – 1.5 A)

To illustrate the proposed model with better performance to characterize MRF VSD than existing models, further investigation is conducted based on the comparison between the proposed model and other model in terms of reconstructed curve and MSE. Here, a hybrid model, reported in (Royel *et al.* 2015), is employed as the comparison object. Its mathematical expression is shown in Eq. (19).

$$T(\theta) = \begin{cases} \delta + \varepsilon \cdot \tanh(\varphi \cdot \dot{\theta}) + \lambda \cdot e^{-\frac{\dot{\theta}^2}{2\sigma^2}}, \ddot{\theta} \geq 0 \\ \delta + \varepsilon \cdot \tanh(\varphi \cdot \dot{\theta}) - \lambda \cdot e^{-\frac{\dot{\theta}^2}{2\sigma^2}}, \ddot{\theta} \geq 0 \end{cases} \quad (19)$$

where δ, ε, φ, λ and σ are identified parameters in the model. Figs. 17 and 18 give the comparisons between experimental and reconstructed responses from both the proposed and hybrid models respectively, when the MRF VSD is driven by 1 Hz frequency harmonic excitation without any current input. The results show that under small loading amplitude (7.06 mm) excitations, the hybrid model has similar modeling accuracy as the proposed model. However, when the loading amplitude is increased to 28.2 mm, the hybrid model is not capable of accurately capturing the device responses. Especially at the saturation areas (circled in the figure), the reconstructed response has obvious deviations. On the contrary, torque outputs from the proposed model

Table 1 MSEs of both proposed and hybrid models for all loading conditions

Loading condition			MSE		Loading condition			MSE	
Frequency	Amplitude	Current	Proposed	Hybrid	Frequency	Amplitude	Current	Proposed	Hybrid
0.5 Hz	7.06 mm	0 A	0.0019	**0.0013**	1 Hz	7.06 mm	0 A	**0.0006**	0.0038
		0.5 A	0.0046	**0.0042**			0.5 A	**0.0029**	0.0153
		1 A	**0.0184**	0.0199			1 A	**0.0153**	0.0747
		1.5 A	**0.0303**	0.1098			1.5 A	**0.0186**	0.0915
		2 A	**0.0710**	0.3704			2 A	**0.0264**	0.1489
	17.65 mm	0 A	0.0011	**0.0009**		17.65 mm	0 A	**0.0003**	0.0095
		0.5 A	**0.0082**	0.0246			0.5 A	**0.0044**	0.0254
		1 A	**0.0507**	0.1783			1 A	**0.0294**	0.0933
		1.5 A	**0.1128**	0.2548			1.5 A	**0.1055**	0.3661
		2 A	**0.1654**	0.4872			2 A	**0.1589**	0.4387
	28.2 mm	0 A	**0.0008**	0.0111		28.2 mm	0 A	**0.0003**	0.0118
		0.5 A	**0.0132**	0.0582			0.5 A	**0.0073**	0.0247
		1 A	**0.0902**	0.2391			1 A	**0.0729**	0.1701
		1.5 A	**0.2051**	0.5113			1.5 A	**0.1965**	0.4465
		2 A	**0.3375**	0.7205			2 A	**0.3318**	0.7743
2 Hz	7.06 mm	0 A	**0.0003**	0.0047	3 Hz	7.06 mm	0 A	0.0007	**0.0006**
		0.5 A	**0.0021**	0.0085			0.5 A	0.0043	**0.0041**
		1 A	**0.0146**	0.0481			1 A	**0.0181**	0.0564
		1.5 A	**0.0176**	0.0636			1.5 A	**0.0205**	0.0931
		2 A	**0.0474**	0.2005			2 A	**0.0306**	0.1982
	17.65 mm	0 A	**0.0003**	0.0084		17.65 mm	0 A	**0.0011**	0.0098
		0.5 A	**0.0032**	0.0192			0.5 A	**0.0042**	0.0279
		1 A	**0.0267**	0.1537			1 A	**0.0422**	0.2035
		1.5 A	**0.0748**	0.3109			1.5 A	**0.0848**	0.3821
		2 A	**0.1274**	0.5673			2 A	**0.1777**	0.6320
	28.2 mm	0 A	**0.0013**	0.0104		28.2 mm	0 A	**0.0011**	0.0095
		0.5 A	**0.0062**	0.0628			0.5 A	**0.0102**	0.0753
		1 A	**0.0708**	0.2367			1 A	**0.0362**	0.1905
		1.5 A	**0.2265**	0.5804			1.5 A	**0.0933**	0.4182
		2 A	**0.3797**	0.8164			2 A	**0.1773**	0.6539

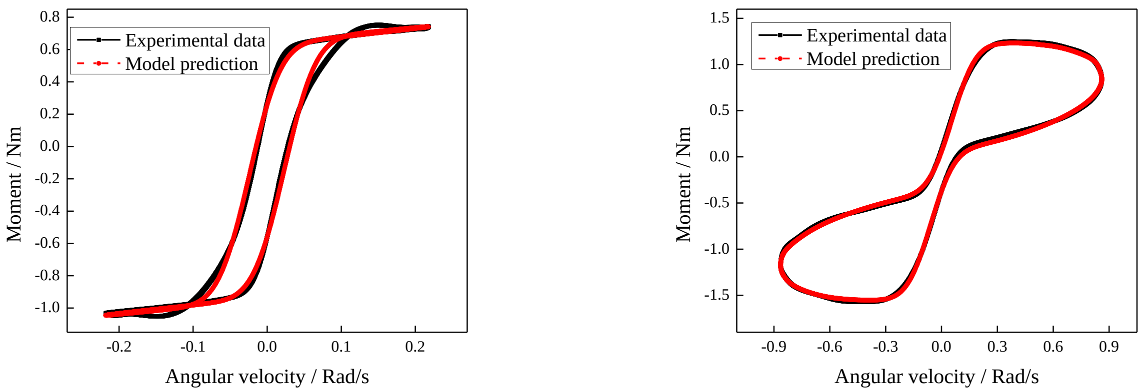

(a) 7.06 mm amplitude (b) 28.5 mm

Fig. 17 Torque-angular velocity response comparisons between experimental data and predictions from the proposed model

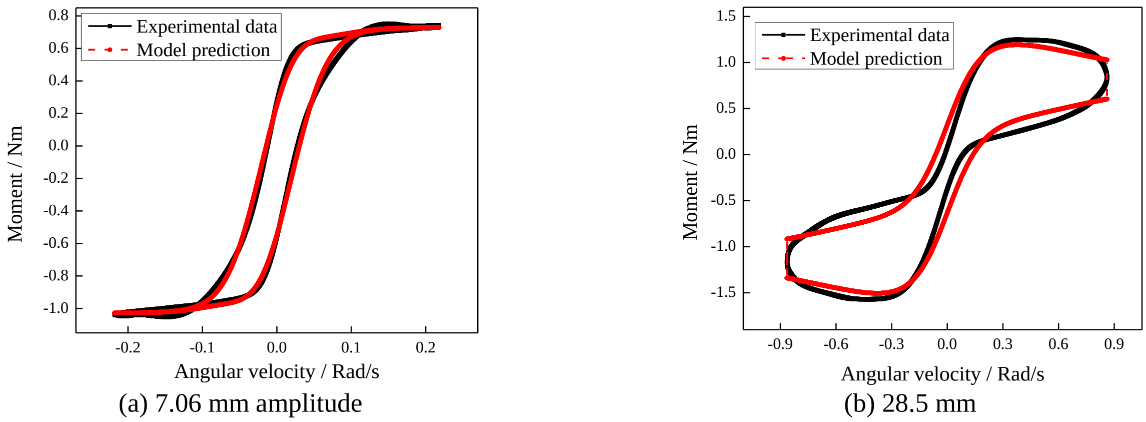

Fig. 18 Torque-angular velocity response comparisons between experimental data and predictions from the hybrid model

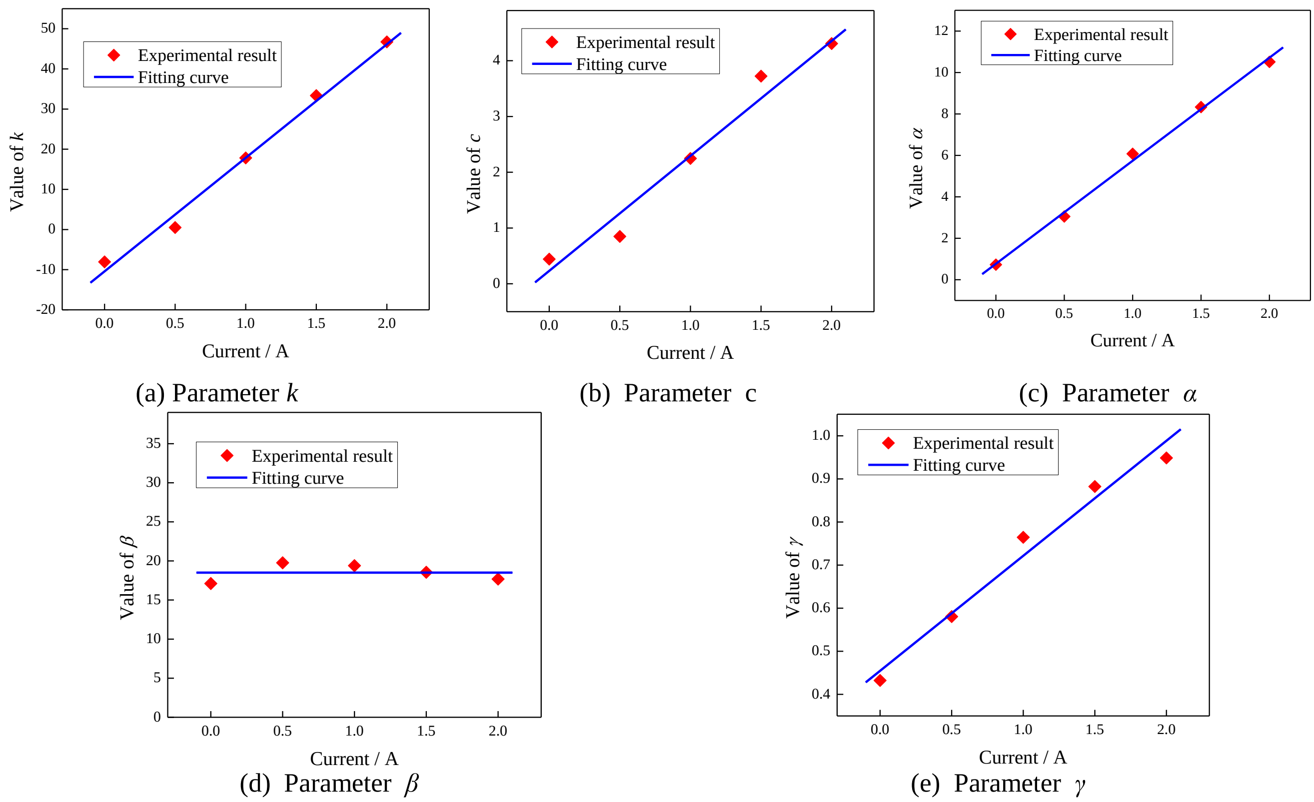

Fig. 19 Relationships between model parameters and current level

still agree well with the experimental results even at large amplitude excitations. Table 1 summarizes the calculated MSEs of both proposed and hybrid models for all the loading conditions. It is observed that the proposed model outperforms the hybrid one for almost all the cases except the cases of 7.06 mm amplitude with 0.5 Hz and 1 Hz frequencies and 0 A and 0.5 A currents as well as 17.65 mm amplitude with 0.5 Hz frequency and 0 A current. Accordingly, compared with the existing model, the proposed rotational hysteresis model could be regarded as a better solution for the design of the feedback controller.

5.3 Generalized rotational hysteresis model

The identification results in Section 5.2 indicate that parameter values of the proposed model are closely associated with the loading condition, including excitation frequency, amplitude and applied electricity current. However, in the practical application, it is unnecessary to obtain the relationships between model parameters and loading frequency and amplitude, as the external excitation is always changeable and uncontrollable. Therefore, only current-dependent property of the model is desirable to implement the adaptive control of output torque resistance of the device. In this case, the parameters estimated from the rotational hysteresis model with various loading conditions are divided into different groups corresponding to different supplying currents. Next, the mean values of the parameter values are calculated at each current level, depicted in Fig. 19. The result in the figure clearly indicates that all the parameters have the almost linear relationships with current level, which may be expressed by 1st-order polynomial functions. It is noticeable from Fig. 19(a) that the rotational stiffness (parameter *k*) of the device shows significant change (500% increases) with the increase of applied current, sufficiently verifying the capacity of the developed VSD. Then, Curve Fitting Toolbox in MATLAB is employed to identify the coefficient values of polynomial functions with the following results.

$$k(I) = -10.41 + 28.48 \cdot I \tag{20}$$

$$c(I) = 0.2324 + 2.061 \cdot I \tag{21}$$

$$\alpha(I) = 0.7702 + 4.971 \cdot I \tag{22}$$

$$\beta(I) = 18.51 \tag{23}$$

$$\gamma(I) = 0.4547 + 0.2669 \cdot I \tag{24}$$

Hence, a generalized model with current-dependent parameters is established with the following expression

$$T_M = k(I) \cdot \theta + c(I) \cdot \dot{\theta} + \alpha(I) \cdot \mathrm{erf}\left[\beta(I) \cdot \dot{\theta} + \gamma(I) \cdot sign(\theta)\right] \tag{25}$$

To demonstrate the effectiveness of this model, Fig. 20 shows the tracking performance of the generalized hysteresis model along time from various applied currents at 0 A, 0.5 A, 1 A, 1.5 A and 2 A and harmonic excitations with 1 Hz frequency and 17.65 mm amplitude.

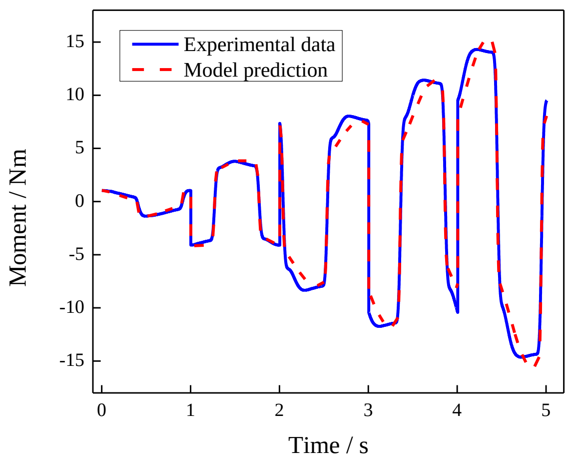

Fig. 20 Comparison between experimental data and the generalized rotational hysteresis model outputs for different applied currents (1 Hz – 17.65 mm)

The comparison result indicates that the torque output from the generalized model well agrees with the measured torques and the model is capable of well capturing the nonlinear dynamics of MRF VSD. This outcome demonstrates the reliability and feasibility of this current-dependent model for its application in the vibration controller design for beam structure using MRF VSDs.

6. Conclusions

This paper presented a rotational hysteresis model to demonstrate the nonlinear and hysteretic behavior of MRF VSD. This new model comprises a rotational spring, a viscous dashpot and a nonlinear hysteresis component with advantages of simple expression, few parameters and efficient computation. Model parameter identification can be considered as solving a global optimization problem, in which the error between experimental data and model prediction is used as the objective function. The solution of optimization problem was realized using a modified evolutionary algorithm based on WOA, in which the nonlinear parameter update strategy is introduced into conventional WOA to prevent the local optimal solution. The experimental data collected from an MRF VSD prototype with various loading conditions were employed for modeling validation. The result verifies that the proposed model is able to characterize the unique features of this device. The comparative studies were also conducted to indicate the superiorities of the proposed model and MWOA over existing MRF VSD model and optimization algorithms in terms of reconstructed response, MSE and convergence rate. Finally, a generalized rotational hysteresis model, based on the current-dependent property of the device, was established and evaluated with outstanding results. Accordingly, it is capable of being applied to the design of the controller for the real-time adaptive vibration control of intelligent structures equipped with MRF VSDs.

Acknowledgments

This research was supported by the Discovery Project (Grant No. DP150102636) from Australian Research Council and Blue Sky Project from University of Technology Sydney. The authors are thankful to the funding bodies.

References

Braz-César, M.T. and Barros, R.C. (2018), "Semi-Active fuzzy based control system for vibration reduction of a SDOF structure under seismic excitation", *Smart Struct. Syst.*, **21**(4), 389-395. https://doi.org/10.12989/sss.2018.21.4.389.

Chen, Z.H., Ni, Y.Q. and Or, S.W. (2015), "Characterization and modeling of a self-sensing MR damper under harmonic loading", *Smart Struct. Syst.*, **15**(4), 1103-1120. https://doi.org/10.12989/sss.2015.15.4.1103.

Christie, M.D., Sun, S., Deng, L., Ning, D.H., Du, H., Zhang, S.W.

and Li, W.H. (2019), "A variable resonance magnetorheological-fluid-based pendulum tuned mass damper for seismic vibration suppression", *Mech. Syst. Signal Pr.*, **116**, 530-544. https://doi.org/10.1016/j.ymssp.2018.07.007.

Dyke, S.J., Spencer, Jr., B.F., Sain, M.K. and Carlson, J.D. (1996), "Modeling and control of magnetorheological dampers for seismic response reduction", *Smart Mater. Struct.*, **5**(5), 565-575.

Dyke, S.J., Spencer, Jr., B.F., Sain, M.K. and Carlson, J.D. (1998), "An experimental study of MR dampers for seismic protection", *Smart Mater. Struct.*, **7**(5), 693-703.

Ehrgott, R.C. and Masri, S.F. (1992), "Modelling of oscillatory dynamic behavior of electrorheologkal materials in shear", *Smart Mater. Struct.*, **1**(4), 275-285.

Fesharaki, J.J. and Golabi, S. (2016), "A novel method to specify pattern recognition of actuators for stress reduction based on particle swarm optimization method", *Smart Struct. Syst.*, **17**(5), 725-742. https://doi.org/10.12989/sss.2016.17.5.725.

Gong, X., Guo, C., Xuan, S., Liu, T. and Peng, C. (2012), "Oscillatory normal forces of magnetorheological fluids", *Soft Matter.*, **8**(19), 5256-5261.

Hong, S.R., Choi, S.B., Choi, Y.T. and Wereley, N.M. (2005), "Non-dimensional analysis and design of a magnetorheological damper", *J. Sound Vib.*, **288**(4-5), 847-863. https://doi.org/10.1016/j.jsv.2005.01.049.

Hu, W. and Wereley, N.M. (2008), "Hybrid magnetorheological fluid-elastomer lag dampers for helicopter stability augmentation", *Smart Mater. Struct.*, **17**(4), 045021.

Huang, J., Zhang, J.Q., Yang, Y. and Wei, Y.Q. (2002), "Analysis and design of a cylindrical magneto-rheological fluid brake", *J. Mater. Process. Tech.*, **129**(1-3), 559-562. https://doi.org/10.1016/S0924-0136(02)00634-9.

Imaduddin, F., Mazlan, S.A. and Zamzuri, H. (2013), "A design and modelling review of rotary magnetorheological damper", *Mater. Design*, **51**, 575-591. https://doi.org/10.1016/j.matdes.2013.04.042

Jiménez, R. and Á lvarez-Icaza, L. (2005), "LuGre friction model for a magnetorheological damper", *Struct. Control Health.* **12**(1), 91-116. https://doi.org/10.1002/stc.58.

Kaveh, A. and Ghazaan, M.I. (2017), "Enhanced whale optimization algorithm for sizing optimization of skeletal structures", *Mech. Based Des. Struct.*, **45**(3), 345-362. https://doi.org/10.1080/15397734.2016.1213639.

Li Voti, R. (2018), "Optimization of a perfect absorber multilayer structure by genetic algorithms", *J. Eur. Opt. Soc.-Rapid.*, **14**(1), 11.

Li, W.H. and Du, H. (2003), "Design and experimental evaluation of a magnetorheological brake", *Int. J. Adv. Manuf. Tech.*, **21**(7), 508-515. https://doi.org/10.1007/s001700300060.

Li, W.H., Du, H., Chen, G., Yeo, S.H. and Guo, N. (2003), "Nonlinear viscoelastic properties of MR fluids under large-amplitude-oscillatory-shear", *Rheol. Acta*. **42**(3), 280-286. https://doi.org/10.1007/s00397-002-0285-4.

Li, Y. and Li, J. (2014), "Dynamic characteristics of a magnetorheological pin joint for civil structures", *Front. Mech. Eng.*, **9**(1), 15-33. https://doi.org/10.1007/s11465-014-0283-0.

Li, Z., Chang, C.C. and Spencer Jr., B.F. (2002), "Intelligent technology-based control of motion and vibration using MR dampers", *Earthq. Eng. Eng. Vib.*, **1**(1), 100-110. https://doi.org/10.1007/s11803-002-0013-1.

Mirjalili, S. and Lewis, A. (2016), "The whale optimization algorithm", *Adv. Eng. Softw.*, **95**, 51-67. https://doi.org/10.1016/j.advengsoft.2016.01.008.

Muthalif, A.G.A., Kasemi, H.B., Nordin, N.H.D., Rashid, M.M. and Razali, M.K.M. (2017), "Semi-active vibration control using experimental model of magnetorheological damper with adaptive F-PID controller", *Smart Struct. Syst.*, **20**(1), 85-97. https://doi.org/10.12989/sss.2017.20.1.085.

Nam, T.H. and Ahn, K.K. (2009), "New approach to designing an MR brake using a small steel roller and MR fluid", *J. Mech. Sci. Technol.*, **23**(7), 1911-1923. https://doi.org/10.1007/s12206-009-0301-z.

Nam, Y.J., Moon, Y.J. and Park, M.K. (2007), "Performance improvement of a rotary MR fluid actuator based on electromagnetic design", *J. Intel. Mat. Syst. Str.*, **19**(6), 695-705. https://doi.org/10.1177/1045389X07079463.

Nguyen, P.B. and Choi, S.B. (2011), "A new approach to magnetic circuit analysis and its application to the optimal design of a bi-directional magnetorheological brake", *Smart Mater. Struct.*, **20**(12), 125003.

Nguyen, Q.H. and Choi, S.B. (2010), "Optimal design of an automotive magnetorheological brake considering geometric dimensions and zero-field friction heat", *Smart Mater. Struct.*, **19**(11), 115024.

Park, E.J., Stoikov, D., Falcao da Luz, L. and Suleman, A. (2006), "A performance evaluation of an automotive magnetorheological brake design with a sliding mode controller", *Mechatronics*, **16**(7), 405-416. https://doi.org/10.1016/j.mechatronics.2006.03.004.

Royel, S., Yu, Y., Li, Y., Li, J. and Ha, Q. (2015), "A hysteresis model and parameter identification for MR pin joints using immune particle swarm optimization", *Proceedings of the 11th International Conference on Automation Science and Engineering*, Gothenburg, Sweden, August.

Sohn, J.W., Oh, J.S. and Choi, S.B. (2015), "Design and novel type of a magnetorheological damper featuring piston bypass hole", *Smart Mater. Struct.*, **24**(3), 035013.

Song, B.K., Nguyen, Q.H., Choi, S.B. and Woo, J.K. (2013), "The impact of bobbin material and design on magnetorheological brake performance", *Smart Mater. Struct.*, **22**(10), 105030.

Spencer, Jr, B.F., Dyke, S.J., Sain, M.K. and Carlson, J.D. (1997), "Phenomenological model for magnetorheological dampers", *J. Eng. Mech.*, **123**(3), 230-238. https://doi.org/10.1061/(ASCE)0733-9399(1997)123:3(230).

Sun, S., Yang, J., Li, W., Deng, H., Du, H. and Alici, G. (2015), "Development of a novel variable stiffness and damping magnetorheological fluid damper", *Smart Mater. Struct.*, **24**(8), 085021.

Sun, W.Z., Wang, J.S. and Wei, X. (2018), "An improved whale optimization algorithm based on different searching paths and perceptual disturbance", *Symmetry*, **10**(6), 210. https://doi.org/10.3390/sym10060210.

Truong, D.Q. and Ahn, K.K. (2010), "Identification and application of black-box model for a self-sensing damping system using a magneto-rheological fluid damper", *Sensor Actuat. A-Phys.*, **161**(1-2), 305-321. https://doi.org/10.1016/j.sna.2010.04.031.

Tse, T. and Chang, C.C. (2004), "Shear-mode rotary magnetorheological damper for small scale structural control experiments", *J. Struct. Eng.*, **130**(6), 904-911. https://doi.org/10.1061/(ASCE)0733-9445(2004)130:6(904).

Wang, D.H. and Liao, W.H. (2011), "Magnetorheological fluid dampers: a review of parametric modeling", *Smart Mater. Struct.*, **20**(2), 023001.

Wang, X. and Gordaninejad, F. (1999), "Flow analysis of field-controllable, electro-and magneto-rheological fluids using Herschel-Bulkley model", *J. Intel. Mat. Syst. Str.*, **10**(8), 601-608. https://doi.org/10.1106/P4FL-L1EL-YFLJ-BTRE.

Wereley, N.M., Kamath, G.M. and Madhavan, V. (1999), "Hysteresis modeling of semi-active magnetorheological helicopter dampers", *J. Intel. Mat. Syst. Str.*, **10**(8), 624-633. https://doi.org/10.1106/NHLE-FNDL-U243-L8U0.

Yang, G., Spencer Jr., B.F., Carlson, J.D. and Sain, M.K. (2002), "Large-scale MR fluid dampers: Modeling and dynamic

performance considerations", *Eng. Struct.*, **24**(3), 309-323. https://doi.org/10.1016/S0141-0296(01)00097-9.
Yang, G., Spencer, Jr., B.F., Jung, H.J. and Carlson, J.D. (2004), "Dynamic modeling of large-scale magnetorheological damper systems for civil engineering applications", *J. Eng. Mech.*, **130**(9), 1107-1114. https://doi.org/10.1061/(ASCE)0733-9399(2004)130:9(1107).
Yi, T.H., Li, H.N. and Zhang, X.D. (2015), "Health monitoring sensor placement optimization for Canton Tower using virus monkey algorithm", *Smart Struct. Syst.*, **15**(5), 1373-1392. http://dx.doi.org/10.12989/sss.2015.15.5.1373.
Yu, M., Wang, S., Fu, J. and Peng, Y. (2013), "Unsteady analysis for oscillatory flow of magnetorheological fluid dampers based on Bingham plastic and Herschel-Bulkley models", *J. Intel. Mat. Syst. Str.*, **24**(9), 1067-1078. https://doi.org/10.1177/1045389X13476151.
Zhou, Q., Nielsen, S.R.K. and Qu, W.L. (2006), "Semi-active control of three-dimensional vibrations of an inclined sag cable with magnetorheological dampers", *J. Sound Vib.*, **296**(1-2), 1-22. https://doi.org/10.1016/j.jsv.2005.10.028.
Zhou, Z., Meng, S.-P., Wu, J. and Zhao, Y. (2012), "Semi-active control on long-span reticulated steel structures using MR dampers under multi-dimensional earthquake excitations", *Smart Struct. Syst.*, **10**(6), 557-572. https://doi.org/10.12989/sss.2012.10.6.557.
Zhu, X., Jing, X., Cheng, L. (2012), "Magnetorheological fluid dampers: A review on structure design and analysis", *J. Intel. Mat. Syst. Str.*, **23**(8), 839-873. https://doi.org/10.1177/1045389X12436735.

HJ